Chemical Engineering Journal 505 (2025) 159206

Contents lists available at ScienceDirect

Chemical Engineering Journal

journal homepage: www.elsevier.com/locate/cej

Recycling of spent lithium-ion batteries via sulfidation shock

Beikai Zhang, Lanbin Wang, Duanmei Song, Jing Wu, Jiadong Yu *, Jinhui Li

State Key Joint Laboratory of Environment Simulation and Pollution Control, School of Environment, Tsinghua University, Beijing 100084, China

ARTICLE INFO

Keywords:
Spent lithium-ion batteries
Electrothermal metallurgy
Selective sulfidation
Battery metal
Recycling

ABSTRACT

Extracting battery metals from spent lithium-ion batteries (LIBs) is a promising solution to address the crisis in battery material supply and the risk of heavy metal pollution. This study proposes a selective sulfidation shock (SS) strategy for the recovery of battery metals from LIBs. The transient high temperatures (~1000 °C) generated by pulsed direct current induce solid-phase interfacial sulfidation reactions of lithium (Li) in cathode particles, preventing the generation of sulfur-containing flue gases while enhancing the selective recovery of Li metal. The thermal shock causes Li to quickly volatilize and concentrate on the cathode particle surface owing to saturation vapor pressure differences between Li and transition metals, where it reacts with the high-melting-point sulfurizing agent ($CaSO_4$) to produce easily soluble Li_2SO_4. The SS process rapidly achieves the transformation of lithium-containing phases within mere seconds, and the subsequent leaching rate of Li in water increases from 40 % to 89 %, with the leaching kinetics improved by 36 times. In addition, thermal shock also promotes the release of lattice oxygen, thereby synergistically enhancing the reduction leaching of transition metal oxides. A comprehensive life cycle assessment revealed that this SS strategy can reduce greenhouse gas emissions by 22 %-43 % compared to traditional pyrometallurgical and hydrometallurgical processes while also yielding 4.97 USD/kg economic benefits.

1. Introduction

The global market share of electric vehicles (EVs) increased from 2 % in 2018 to 18 % in 2023 owing to advancements in new energy technologies and support from environmental policies [1]. The global demand for lithium-ion batteries (LIBs), as critical components of EVs, surpassed 505 GWh in 2023, marking a 28 % increase as compared to the previous year [2]. However, their typical lifespan, ranging from 3 to 10 years, is expected to lead a substantial wave of LIB retirement worldwide [3], with an estimated 767 GWh of LIBs retired by 2035. Recycling these spent batteries is crucial, as it could reduce the consumption of natural battery metals by 15 %-30 % [4]. In response to this pressing issue, the European Union implemented legislation governing the recovery and disposal of spent LIBs [5], recognizing key materials such as lithium (Li), nickel (Ni), cobalt (Co), and manganese (Mn) as essential resources, mandating local recycling efforts, and prohibiting simple landfilling or cross-border waste transfer [6].

Selective sulfidation, which is based on ion exchange, is recognized as a promising scalable technology for battery metal recovery [7–12]. However, current thermal sulfidation methods require continuous heating at 400 °C-750 °C for 20–180 min to disrupt the layered structure of battery materials [13–18], leading to high energy consumption and a large carbon footprint. Furthermore, the classic sulfidation mechanism involves reactions between battery metals and sulfur gases, such as SO_2, SO_3, or sulfur vapor (S_2), which are produced during the thermal decomposition of sulfurizing agents [19–21]. Although the reaction kinetics are favorable, sulfur-containing flue gases are inevitably released. Therefore, shifting from the existing gas–solid sulfidation system to a solid–solid sulfidation system which is crucial for mitigating the environmental impact of thermal sulfidation methods. Unfortunately, conflict between the thermal stability of solid sulfurizing agents and sulfidation thermodynamics limits the feasibility of solid–solid reactions using traditional heating elements.

Joule heating technology is an innovative electrothermal metallurgical method that utilizes pulsed direct current to rapidly heat materials from 1000 °C-3000 °C within seconds [22–25]. Remarkably, this process consumes only 1/500 of the energy required by traditional tube furnaces and has recently been applied to metal recovery in urban mining. For example, Deng et al. [26] utilized ultrahigh-temperature flash Joule heating (approximately 3400 K) to improve the halogenation and evaporation separation of precious metals in waste circuit boards. This approach capitalized on vapor pressure differences between non-metals

* Corresponding author.
E-mail address: yjd2022@tsinghua.edu.cn (J. Yu).

https://doi.org/10.1016/j.cej.2025.159206
Received 31 October 2024; Received in revised form 18 December 2024; Accepted 1 January 2025
Available online 2 January 2025

and metal halides, such as rhodium (Rh), palladium (Pd), silver (Ag), and gold (Au). However, separating the mixed metals in the resulting vapors remains a substantial challenge. To overcome this issue, Zhu et al. [27] employed high-temperature Joule heating (i.e., sustained heating at approximately 2000 °C for 20 s) to recover battery metals from spent LIBs, converting Li to Li_2O for preferential aqueous extraction and recovering transition metals (TMs) by acid leaching. Although this selective recovery strategy represents some progress, high-temperature shocking can lead to substantial Li volatilization losses and sintering or melting of battery particles, greatly reducing the leachability of battery metals. Therefore, the development of a selective and mild electrothermal treatment is essential to effectively recover battery metals from spent LIBs.

Here, we combine the advantages of sulfidation chemistry and an electrothermal process in the development of a low-temperature sulfidation shock (SS) strategy (Fig. S1). We selected thermally stable gypsum ($CaSO_4{\cdot}2H_2O$) as the electrothermal sulfidation reagent. Fig. S2 illustrates the thermal stability of various sulfidation reagents. In contrast to high-temperature Joule heating technology, the SS process operates at approximately 1000 °C, resulting in Li loss rate of approximately 0.2 %. The transient high temperatures induce Li volatilization and enrichment while simultaneously stimulating a solid–solid sulfidation reaction between Li and $CaSO_4$. The Li leaching kinetics during the SS process were increased 36-fold compared to direct thermal shock at the same temperature, leading to a substantial reduction in leaching equilibrium time. The reduction in TM oxidation states further contributed to successful extraction, with > 95 % recovery of TMs during a two-stage sulfuric acid leaching process under mild conditions (0.5 M, 50 °C). A life cycle assessment demonstrated that the SS strategy significantly reduced total energy consumption, greenhouse gas emissions, and waste discharge, while generating a profit of up to 4.97 USD/kg.

2. Experimental

2.1. Chemicals and materials

Spent NCM ($LiNi_{0.6}Co_{0.2}Mn_{0.2}O_2$) batteries from end-of-life EVs were dismantled and employed as experimental materials. Gypsum ($CaSO_4{\cdot}2H_2O$, AR; MREDA Co., Beijing, China), sodium chloride (NaCl, AR; Sinopharm, Beijing, China), sulfuric acid (H_2SO_4, AR; Tongguang Fine Chemicals, Co., Beijing, China), hydrochloric acid (HCl, AR; Tongguang Fine Chemicals, Co.), and nitric acid (HNO_3, AR; Tongguang Fine Chemicals, Co.) were purchased from the unified reagent management platform of Tsinghua University. Experimental water was provided by the laboratory water purification system (Medium-E600, Shanghai Hitech Instrumens, Co., Shanghai, China).

2.2. Experimental methods

The discharged spent NCM batteries were placed in saturated NaCl solution for 24 h. Subsequently, the batteries were manually dismantled to collect the cathode strips, which were processed by a small crusher into finer particles. The crushed material was subsequently sieved through a 200 mesh screen to obtain cathode powder with particle sizes < 0.074 mm. The chemical composition of the spent NCM powder was listed in Table S1. The cathode powder was mixed with gypsum at a specific ratio using a planetary ball mill at 200 rpm for 30 min to ensure a uniform blend. Next, 500 mg of this mixture was placed into a graphite crucible for SS at 100–140 A for 5–40 s. After SS was complete, deionized water was employed to dissolve Li from the SS products. After Li extraction, the remaining residue was soaked in 0.5 M sulfuric acid to dissolve the TMs. The filtrates obtained at various stages were analyzed to evaluate the respective extraction efficiency (η_i) of Li and TMs, which was calculated using Eq. (1):

$$\eta_i(\%) = [C_i V_i / C_0 V_0] \times 100\% \quad (1)$$

where C_i is the concentration of metal ion "i" in the leachate, V_i is the volume of the leachate, C_0 is the concentration of metal ion "i" in the raw material when dissolved in aqua regia, and V_0 is the volume of aqua regia leachate.

To evaluate the impact of different heating methods on the thermal loss rate of Li, samples after thermal treatment were subjected to microwave digestion, followed by inductively coupled plasma optical emission spectroscopy (ICP-OES) to determine the metal content in the digestion solution. The thermal loss rate of Li (η_{Li}) was calculated using Eq. (2):

$$\eta_{Li}(\%) = [M/M_0] \times 100\% \quad (2)$$

where M is the Li content in the SS products, and M_0 is the Li content in the raw materials.

2.3. Characterization

The metal ion concentrations in the leaching solution were measured by ICP-OES using an OPTIMA 2000 spectrometer (PerkinElmer, Waltham, MA, USA). The crystal structures of the samples were characterized by X-ray diffraction (XRD) using a PW-1700 diffractometer (Philips, Cambridge, MA, USA) with a CuKα radiation source (λ = 0.154 nm) at 40 kV and 30 mA. The thermal process of samples was analyzed by thermogravimetry-Fourier-transform infrared spectroscopy-mass spectrometry (TG-MS-FTIR, Netzsch, X70, Germany. The surface chemical composition of samples was analyzed via X-ray photoelectron spectroscopy (XPS; ULVAC-PHI, Inc., Kanagawa, Japan) with etching times of 0, 10, 60, 120, 180, 240, 360, and 480 s. Time-of-flight secondary ion mass spectrometry (TOF-SIMS) was performed using a TOF.SIMS 5–100 mass spectrometer (ION-TOF GmbH, Münster, Germany). The surface morphology and elemental distribution of samples were characterized via field-emission scanning electron microscopy combined with energy-dispersive spectroscopy using a MERLIN Compact microscope (Carl Zeiss, Jena, Germany) and high-resolution field-emission transmission electron microscopy (HRTEM) using a JEM-2100F microscope (JEOL Ltd., Tokyo, Japan), respectively. Synchrotron X-ray absorption near-edge structure (XANES) spectroscopy was performed at the Shanghai Synchrotron Light Source Facility.

2.4. Economic and environmental analysis

The EverBatt model [28], a closed-loop battery recycling model developed by the Argonne National Laboratory, was employed to compare the techno-economic benefits and life cycle assessment of the pyrometallurgical, hydrometallurgical, and SS recycling processes based on an annual processing capacity of 10,000 tons of spent NCM cells.

3. Results and discussion

3.1. Pre-extraction of lithium from cathode materials via sulfidation shock

The specific electric heating conditions and device structure are illustrated in Fig. 1a and S3. Unlike conventional resistive heating methods, we achieved precise control over the temperature and heat retention time of the graphite support by adjusting the pulse current intensity and duration (Fig. 1b). The material rapidly heated from 25 °C to 1000 °C within approximately 15 s when the current intensity was set to 120 A. This heating rate was 200 to 800-fold faster than that of traditional tube furnaces, which typically operate at rates of 5 °C-20 °C per min. To further demonstrate the advantages of electrothermal sulfidation, the energy consumption of traditional sulfidation roasting were listed in Table S2, which are approximately 167 to 1000-fold higher than

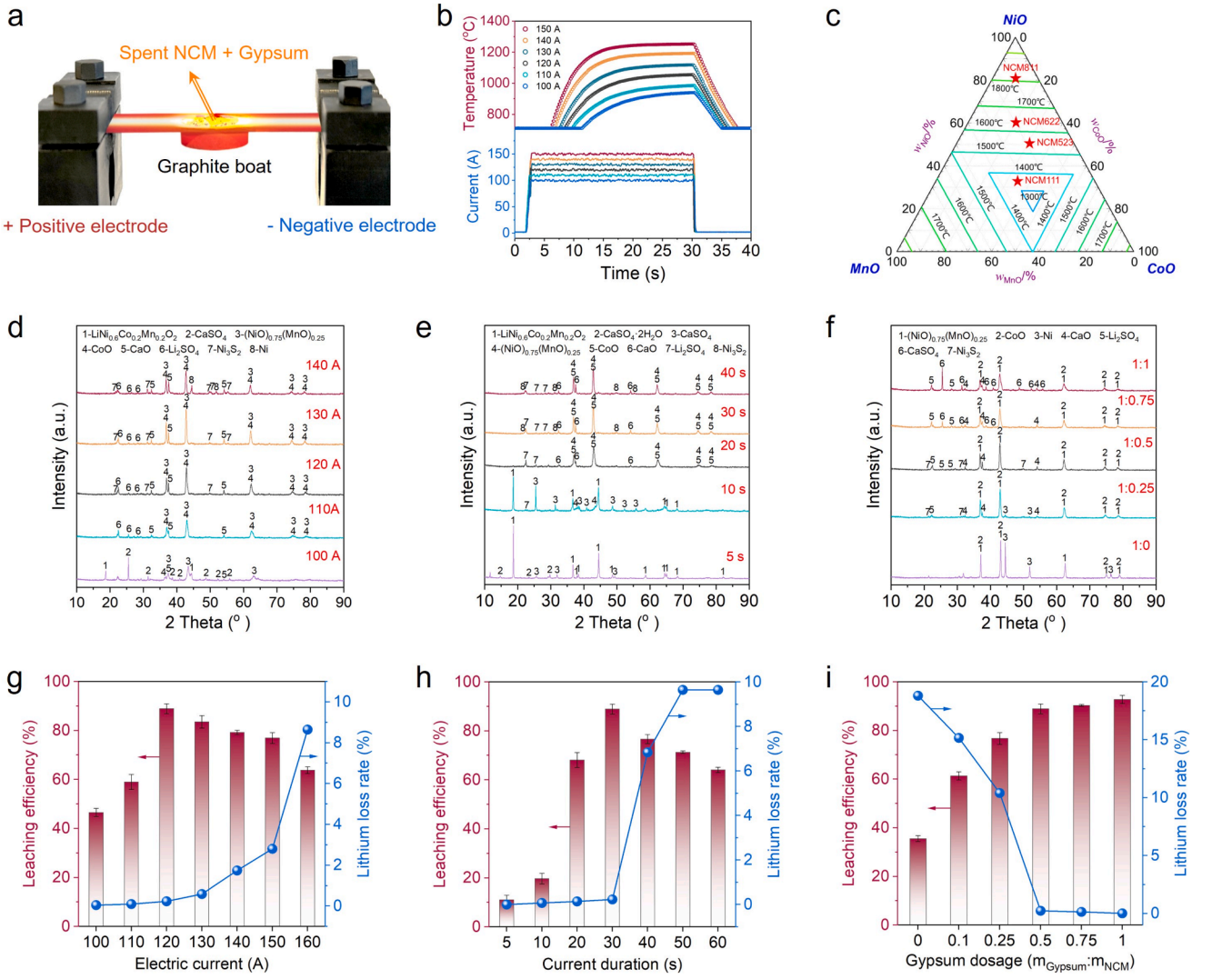

Fig. 1. (a) Schematic illustration of the SS process. (b) Real-time temperature measurement under various current. (c) Melting isotherms of NiO-CoO-MnO slag system. XRD patterns of the sulfidation products with different (d) electric current, (e) current duration and (f) gypsum dosage. Effect of (g) electric current (30 s, Gypsum/NCM mass ratio of 0.5:1), (h) current duration (120 A, Gypsum/NCM mass ratio of 0.5:1), (i) gypsum dosage (120A, 30 s) on water leaching efficiency and thermal loss rate of Li.

those of the SS method,

As shown in Fig. S4a, b, the thermal shock effectively removed crystallization water from gypsum without inducing high-temperature decomposition of $CaSO_4$. This observation aligned with the thermodynamic feasibility presented in Fig. S5. The XRD patterns (Fig. S4c, d) indicated that the (003), (104), and (018) planes of the battery material's having layered structure disappeared with increasing current duration. Concurrently, the (111), (200), and (220) planes of a rock salt structure became visible. This transformation was attributed to the poor thermal stability of the cathode material, wherein TM ions were easily reduced and migrated to Li vacancy sites during heating, resulting in conversion of the poly-crystalline layered structure to a rock salt structure [29,30]. From a chemical perspective, the thermal degradation process of layered $LiTMO_2$ (where TM = Ni, Co, Mn, or $Ni_xCo_yMn_z$, x + y + z = 1) particles during thermal shock can be described as follows:

$$2LiTMO_2(\text{layered}) \rightarrow 2TMO(\text{rock salt}) + Li_2O + 0.5O_2 \quad (3)$$

We employed FactSage 8.3 software [31] to calculate the isothermal melting curves for the NiO-CoO-MnO slag system. As illustrated in Fig. 1c, the melting temperatures for NCM111, NCM523, NCM622, and NCM811 were approximately 1350 °C, 1550 °C, 1630 °C, and 1810 °C, respectively. Thus, the thermal shock temperature must not exceed 1350 °C to ensure SS process continuity and subsequent leaching. Next, we analyzed the phase transformations that occurred when gypsum was mixed with the cathode material before and after SS treatment. As shown in Fig. 1d, the cathode material decomposed into TM oxides at a current intensity of 110 A, with a distinct Li_2SO_4 phase appearing in the XRD pattern at 20°-30°. Peaks associated with Ni_3S_2 and metallic Ni emerged in the XRD pattern as the current intensity increased, which was attributed to carbon materials in the cathode powder (conductive carbon and polyvinylidene fluoride binder) facilitating the sulfurization reduction of NiO, as indicated by the thermodynamic feasibility (Fig. S6a). Furthermore, the NCM cathode completely transformed into TM oxides and Li_2SiO_4 as the current duration increased to 20 s (Fig. 1e).

Moreover, the intensity of the Li_2SO_4 peak in the XRD pattern gradually strengthened with increasing amount of gypsum (Fig. 1f), indicating that water leaching of Li became more effective. Under optimal leaching conditions (30 min, liquid/solid ratio of 10:1, and 25 °C), we further evaluated how the SS conditions affected Li extraction efficiency, revealing that increasing the current intensity (Fig. 1g) and duration (Fig. 1h) enhanced the Li leaching rate. However, excessively high current intensities (>120 A) and prolonged durations (>30 s)

resulted in thermal volatilization losses of Li. Notably, as depicted in Fig. 1i, the thermal loss of Li significantly decreased from 18.8 % to 0.23 % when the gypsum/NCM mass ratio increased from 0 to 0.5. This result suggested that gypsum acted as a thermal buffer during the thermal shock owing to its lower thermal conductivity (0.2–0.4 W $m^{-1}K^{-1}$) compared to that of the cathode material (1–10 W $m^{-1}K^{-1}$). In contrast to traditional sulfidation methods conducted in a tube furnace (Fig. S7), the rapid heating and cooling rates achieved through Joule heating initiated the sulfidation of Li and greatly minimized its thermal volatilization losses. Under optimized SS conditions (120 A, 30 s, and gypsum/NCM mass ratio of 0.5), we achieved Li leaching rate of 89 %, with a minimal thermal loss rate of Li of only 0.23 %. Importantly, the Ni, Co, and Mn ion concentrations in the Li extraction solution were below ICP-OES detection limits (1–10 ppb), indicating that the SS process enabled selective recovery of Li while minimizing recovery of unwanted metals.

3.2. *Leaching kinetics and selective sulfidation thermodynamics*

This study investigated the water leaching kinetics of SS products and compared them with those resulting from carbothermal shock (approximately 1000 °C for 30 s) and raw cathode materials (direct leaching without pre-treatment). As illustrated in Fig. 2a, the Li leaching rate for the SS products reached 70.1 % within 30 s. By contrast, the Li leaching rates for the carbothermal shock products and raw electrode materials were only 43.2 % and 6.6 %, respectively, even after 60 min (Fig. S8). During the carbothermal shock process, Li is converted to Li_2CO_3 (Fig. S4c, d), which has a solubility of only 12.8 g/L at 25 °C [14,32]. Thus, we employed a high liquid-to-solid ratio of 50:1 to enhance Li extraction from the carbothermal shock products. However, this approach resulted in a maximum Li concentration of only 1.07 g/L in the leachate (Fig. S9). We further analyzed the relationship between the Li leaching rate and changes in reactant concentrations across various materials (refer to Supplementary Note 4 in reference [23] for the fitting methodology). Due to the high solubility of Li_2SO_4 (Fig. S10), the high dissolution rate of Li from the SS products was maintained for a longer period of time compared to that from the carbothermal shock products and raw electrode materials, lasting until the end of the reaction (Fig. 2b). In the initial stages of Li extraction (approximately 10 s), the leaching rate of the SS products was approximately 5-fold faster than that of the carbothermal shock products and approximately 36-fold

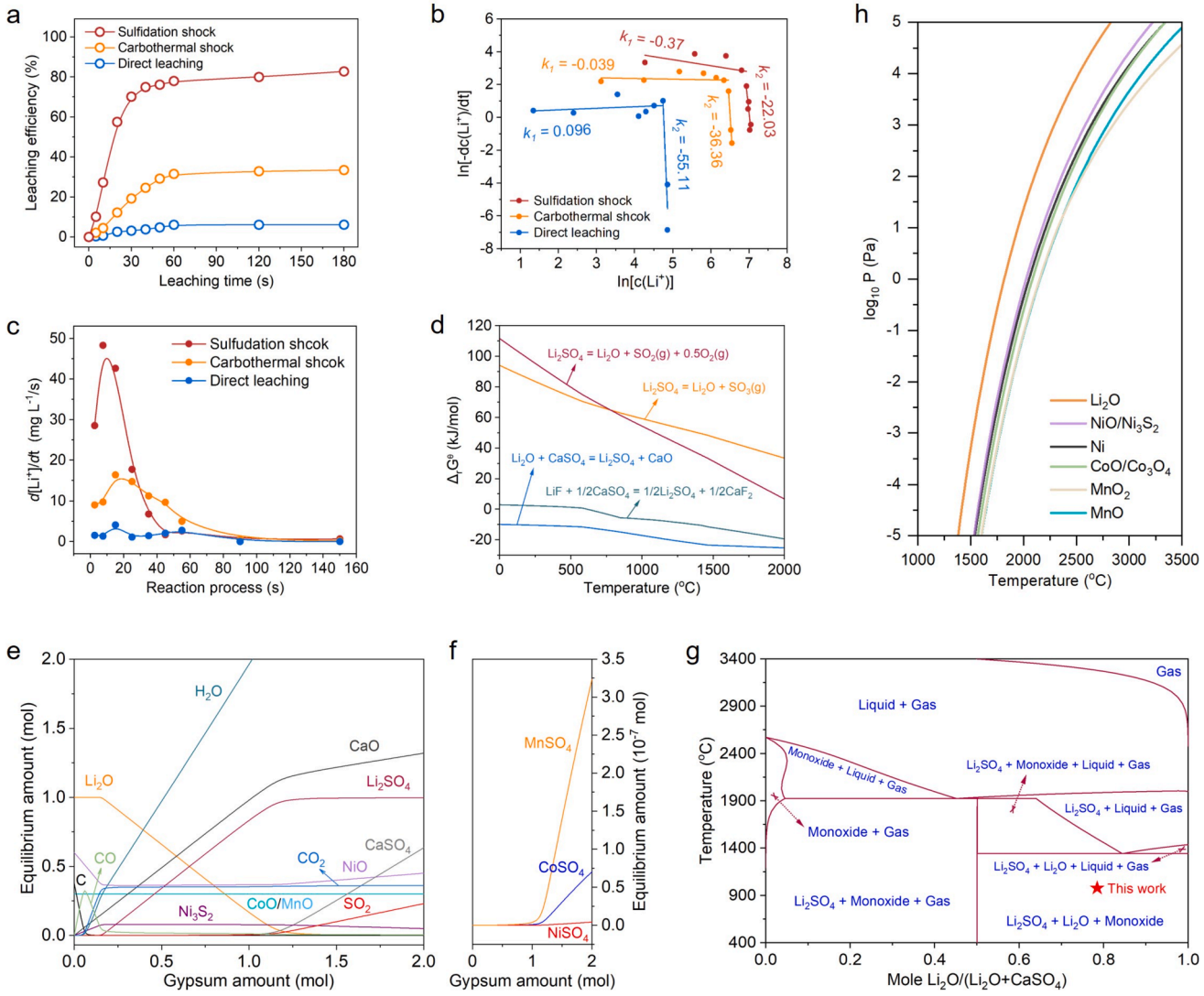

Fig. 2. (a) Effect of leaching time on the leaching efficiency of Li (conditions: 25 °C, liquid–solid ratio of 10:1). (b) Relationship between kinetic Li leaching efficiency and the concentration of Li^+ in the leachate. (c) Dissolution rate of Li from spent NCM in different treatment methods at 25 °C. (d) The Gibbs free energy change ($\Delta_r G^\theta{}_T$) of possible thermodynamic reactions during the sulfidation shock. (e-f) Equilibrium compositions of the sulfidation products at 1000 °C. (g) Phase diagram of Li_2 O-$CaSO_4$ system (adapted from FactSage thermochemical software and databases [31]). (h) Vapor pressure–temperature relationship of battery metal compounds (calculated by Factsage 8.3).

faster than that of the raw cathode materials. The rapid dissolution rate significantly reduced the reaction termination time, as shown in Fig. 2c.

This study assessed the thermodynamic behavior of sulfidation reactions for battery metals. Fig. 2d presents the Gibbs free energy change (Δ_rG^{θ}) for the solid–solid reaction between Li_2O and LiF (derived from the electrolyte) with $CaSO_4$ at approximately 1000 °C, which was found to be < 0 kJ/mol. The high thermal stability of Li_2SO_4 was a prerequisite for the high-temperature solidification of Li. By contrast, the Δ_rG^{θ} values for the TM oxides were > 0 kJ/mol (Fig. S6b-f), indicating that only the sulfidation reaction involving Li components could spontaneously occur. The multiphase thermal equilibrium calculations clearly illustrated phase component changes during the SS process, with detailed calculations provided in Table S3. As shown in Fig. 2e, increasing the amount of gypsum led to a gradual conversion of Li_2O into Li_2SO_4, whereas TM oxides did not transform into sulfates. Even when 2 mol of gypsum were added, the equilibrium concentrations of $NiSO_4$ (4.1×10^{-9} mol), $CoSO_4$ (7.02×10^{-8} mol), and $MnSO_4$ (3.2×10^{-7} mol) in the system were minimal (Fig. 2f). The strength of the metallicity of the metal elements, determined based on their first ionization energy, was in the following order: Li (5.39 eV) > Ca (6.11 eV) > Mn (7.43 eV) > Ni (7.64 eV) > Co (7.88 eV) [33]. Therefore, only Li was capable of displacing the highly electronegative sulfate ions from $CaSO_4$. These thermodynamic calculations confirmed the feasibility of selective sulfidation during the SS process. Moreover, sulfur-free emissions could be achieved during the SS process by controlling the amount of gypsum added. The production of SO_2 and SO_3 was limited to only 4.6×10^{-3} and 5.4×10^{-20} mol, respectively, when 1 mol of gypsum was incorporated (Fig. 2e), which aligned with the results obtained via TG-FTIR-MS (Fig. S11).

The phase transition trends of Li during high-temperature metallurgy were analyzed using the Li_2O-$CaSO_4$ binary phase diagram. As illustrated in Fig. 2g, increasing temperature resulted in the formation of Li-containing gas and liquid phases within the metallurgical melt. Controlling the temperature and quantity of gypsum was crucial to reducing Li losses due to metal vaporization. Fortunately, no phase transitions of Li occurred within the equilibrium system during the SS process at 400 °C-1345 °C. Fig. 2h demonstrates that the saturation vapor pressures of Li_2O were higher than those of the TM oxides, indicating that Li had a greater tendency than TM oxides to volatilize at high temperatures. This finding provides a theoretical foundation for understanding

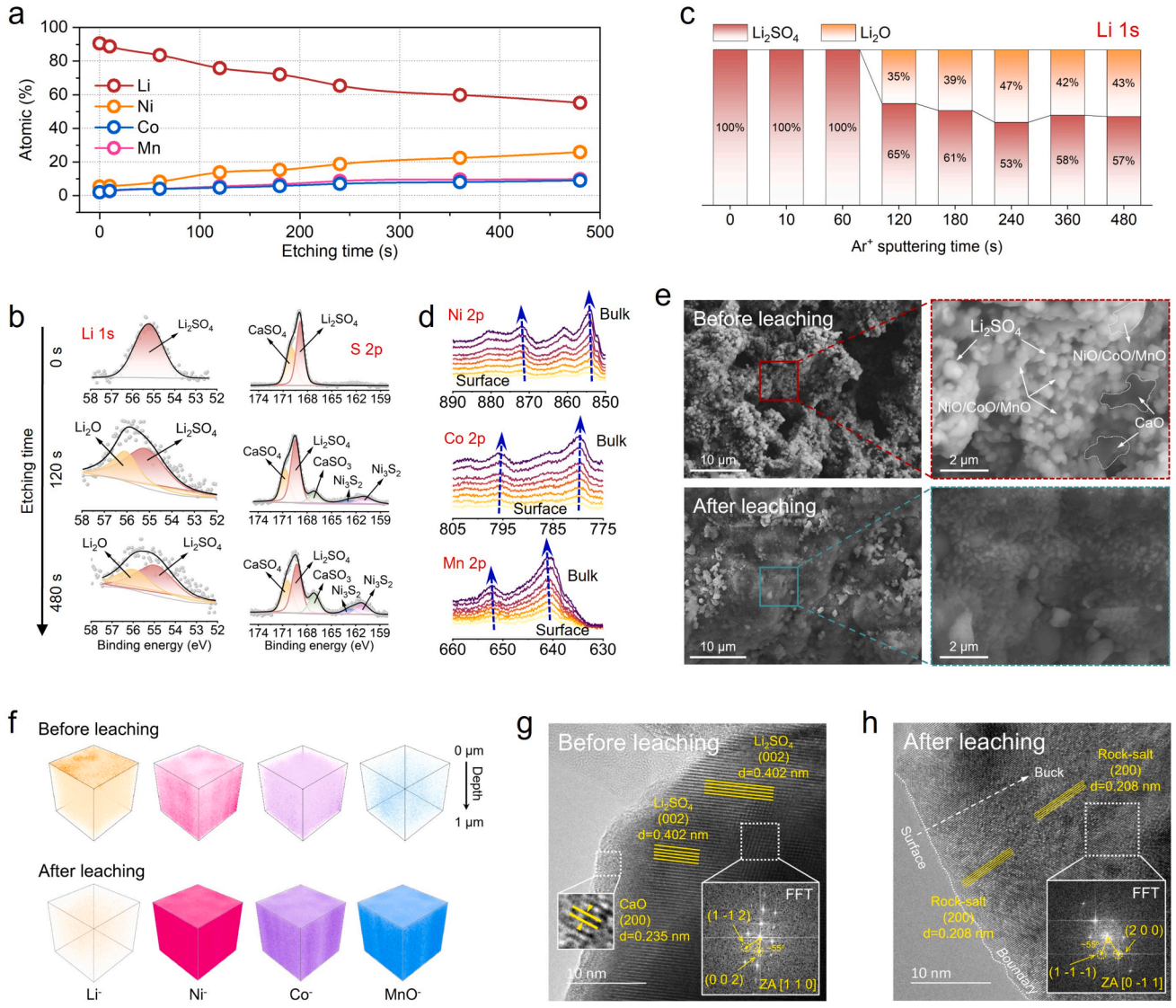

Fig. 3. (a) Atomic ratio of elements in the SS products at different XPS etching times. XPS spectra of different elements at different depths in the SS products: (b) Li 1 s and S 2p (the chemical equation involving the transformation of $CaSO_3$ is $2CaSO_4 + C = 2CaSO_3 + CO_2$, and the $\Delta_r G^{\theta}$ is less than 0 kJ/mol at temperatures above 572 °C), (d) the Co 2p, the Mn 2p and the Ni 2p. (c) Li_2SO_4 /Li_2O ratio as the XPS etching time is increased in the SS products. Microstructure characterization of the SS products before and after Li extraction: (e) SEM images, (f) TOF-SIMS three-dimensional images, and (g-h) HRTEM-FFT images.

the Li volatilization behavior prior to sulfidation.

3.3. Mechanisms of sulfidation concentration of lithium

The migration behavior of elements in battery metals during SS was studied using XPS. As illustrated in Fig. 3a, the relative Li content in the SS products decreased with greater etching depth during the XPS analysis, whereas the relative TM content exhibited only a slight increase, indicating that Li moved from the particle interior to its surface during the thermal shock process. The high-resolution XPS spectrum of Li 1 s (Fig. 3b) revealed that only Li_2SO_4 (55.2 eV) was detected on the SS product surface, although the characteristic peak of Li_2O (56.1 eV) appeared in the Li 1 s spectrum with increasing etching depth. The proportion of Li_2SO_4 decreased from 100 % to 57 % over a continuous XPS etching period of 0–480 s (Fig. 3c). The S 2p XPS spectrum (Fig. 3b) further confirmed that only Li_2SO_4 (168.9 eV) and $CaSO_4$ (169.9 eV) were present on the particle surface, whereas Ni_3S_2 (162.7 and 160.9 eV) and $CaSO_3$ (167.1 eV) were detected in the interior. The proportion of Li_2SO_4 in the S 2p spectrum decreased from 58 % to 41 % after 480 s of etching (Fig. S12), supporting the interfacial sulfidation behavior of Li. Additionally, the characteristic peaks in the Ni 2p, Co 2p, and Mn 2p spectra shifted toward binding energies associated with higher valence states with increasing etching depth (Fig. 3d), indicating that the external structure of the cathode material underwent preferential damage during the SS process.

SEM and HRTEM were used to observe the changes in morphology and microstructure of the SS products before and after Li extraction. Fig. 3e demonstrates that the surface of the SS products was uniformly covered with white spherical particles, which disappeared following water leaching. Semiquantitative energy-dispersive spectroscopy point analysis on these characteristic areas revealed that the primary component of the white spherical particles was Li_2SO_4, based on the atomic ratios of Ca, S, and O (Fig. S13). The SEM mapping results (Fig. S14) confirmed that Ni, Co, and Mn were present in the leaching residual, whereas the S signal strength was decreased. To detect changes in elemental intensity in the sulfidation shock products before and after Li extraction, we employed the time-of-flight secondary ion mass spectrometry (TOF-SIMS). Three-dimensional imaging (Fig. 3f), depth profiles (Fig. S15a, b), and surface distribution maps (Fig. S15c) revealed that the Li signal in the SS products decreased with increasing etching depth and nearly disappeared after leaching. Additionally, Ni, Co, and Mn signals in the leachate exhibited uniform high-density distribution (Fig. 3f), indicating that Li rapidly migrated to the particle surface during the SS process, whereas no interfacial TM migration occurred. HRTEM images of the SS products (Fig. 3g) revealed an interplanar spacing of 0.402 nm at the particle surface, which corresponded to the (002) plane of Li_2SO_4. Fast Fourier transform (FFT) of the images aligned with the classical pattern of Li_2SO_4, confirming Li_2SO_4 shell formation during the SS process. The lattice fringe of 0.235 nm observed on the particle surface corresponds to the (002) crystal plane of the sulfidation by-product phase (CaO). Therefore, thermal sulfidation of Li by $CaSO_4$ could be represented by the chemical equation: $Li_2O + CaSO_4 = Li_2SO_4 + CaO$. HRTEM images of the leachate (Fig. 3h) revealed a lattice spacing of 0.208 nm for the particle surface and in interior, corresponding to the (200) plane of rock salt, which was attributed to high-temperature decomposition of the cathode material. Additionally, the smooth edges of the leachate particles suggested that all soluble substances were dissolved within the SS products (Fig. 3h).

3.4. Improved Extractability of transition metals by sulfidation shock

Traditional acid leaching methods require the reduction of higher metal ion oxidation states in the cathode material before battery metals can be dissolved. By contrast, the TMs in the SS products dissolved directly in dilute sulfuric acid (0.5 M) without further reduction. As shown in Fig. 4a, the SS process significantly enhanced the acid leaching efficiency of TMs. The TM extraction rates were 97.7 %, 99.5 %, and 94.9 % for Ni, Co, and Mn, respectively, after an approximate time of 40 min. The total extraction rate was approximately 2.2-fold higher than that obtained through direct acid leaching. The kinetic results indicated that the initial dissolution rate of TMs in the leachate increased by approximately 60 % compared to direct acid leaching (Fig. S16), and the correlation between the reaction rate and TM concentration (k) was lower, suggesting the occurrence of a more stable acid leaching process. Furthermore, the leaching efficiency of TMs significantly increased with increasing temperature but decreased with increasing solid-to-liquid ratio (Fig. 4b).

The reduction of TM valence states greatly enhances the thermodynamic feasibility of acid dissolution reactions for battery metals [23,27]. Thus, we calculated the Δ_rG^θ values for the acid dissolution reactions of different TM oxidation states at 50 °C. As illustrated in Fig. 4c and detailed in Table S4, the spontaneity of TM oxides dissolving in sulfuric acid increased with decreasing TM valence state. XPS analysis of TM valence components of TMs elements within 5 nm of the surface before and after the SS process (Fig. S17) revealed that the Ni^{3+}/Ni^{2+}, Co^{3+}/Co^{2+}, and Mn^{4+}/Mn^{2+} ratios in the SS products decreased by 0.3, 0.78, and 0.24, respectively. Additionally, TG-MS analysis of the cathode material revealed a strong signal for $^{32}O^{2+}$ (Fig. S11e), suggesting that electrons migrated from the O 2p orbitals in the TM-O covalent bonds to higher-valent TM ions, resulting in the reduction of TMs and oxidation of lattice oxygen [34,35].

To further investigate the thermal degradation process of the cathode material, we employed hard X-ray absorption spectroscopy (HXAS) to quantitatively analyze the valence state composition of the particles before and after the SS process. Given the structural similarities among TMs in the cathode material, we focused our analysis on Co. The Co K-edge XANES spectra for the SS products (Co-SS), raw materials (Co-RM), and standard Co metal oxides are presented in Fig. 4d. The absorption edge of Co-SS closely aligned with that of CoO, exhibiting a decrease of approximately 1.7 eV compared to Co-RM. This shift indicated a reduction in the oxidation state of Co following the SS process. Further fitting analysis of the valence state of Co atoms, as shown in Fig. 4e and S18, indicated that the average oxidation states of Co in the cathode materials from spent LIBs after the SS process decreased from + 2.32 to + 2.05, and the Co^{2+} content increased from 15.1 % to 100 %. Further, we analyzed the chemical and structural characteristics of Co via FT of the extended X-ray absorption fine structure (EXAFS) data at the Co R-edge. Fig. 4f demonstrates that the FT spectrum displayed two prominent peaks, with the first (1.49 and 1.59 Å) and second (2.45 and 2.57 Å) peaks corresponding to the Co-O and Co-Co coordination shells, respectively. Notably, the coordination distances of Co-O and Co-M (where M = Ni, Mn, Co) in the SS products increased compared to those in particles before the SS process, and the amplitude of Co-O significantly decreased. This finding indicated that thermal degradation led to excess disorder of Co^{2+} [36–38]. To precisely assess the changes in bond lengths and coordination numbers of Co atoms following the SS process, we quantitatively analyzed the EXAFS fitting curves using the least squares method. As depicted in Fig. 4g and summarized in Table S5, the bond lengths around Co atoms increased with the degree of oxygen loss in the cathode material [39,40]. Specifically, the Co-O bond length expanded from 1.91 ± 0.01 to 2.08 ± 0.01 Å, while the coordination number increased from 5.6 ± 0.2 to 6.0 ± 0.4. Similarly, the Co-M bond length increased from 2.86 ± 0.01 to 2.99 ± 0.01 Å, while the coordination number increased from 7.4 ± 0.3 to 12.1 ± 0.4. These results indicated that the thermal shock induced the reduction of Co and compromised the lattice structure integrity in the raw materials. Wavelet transform analysis of the EXAFS data further supported this conclusion (Fig. 4h and S19). The Co K-edge contour map for Co-RM exhibited two peaks of maximum intensity correlating with the scattering of Co_3O_4. By contrast, the atomic distance and amplitude of Co-O in Co-SS notably changed, with its two-dimensional profile aligning closely with CoO scattering.

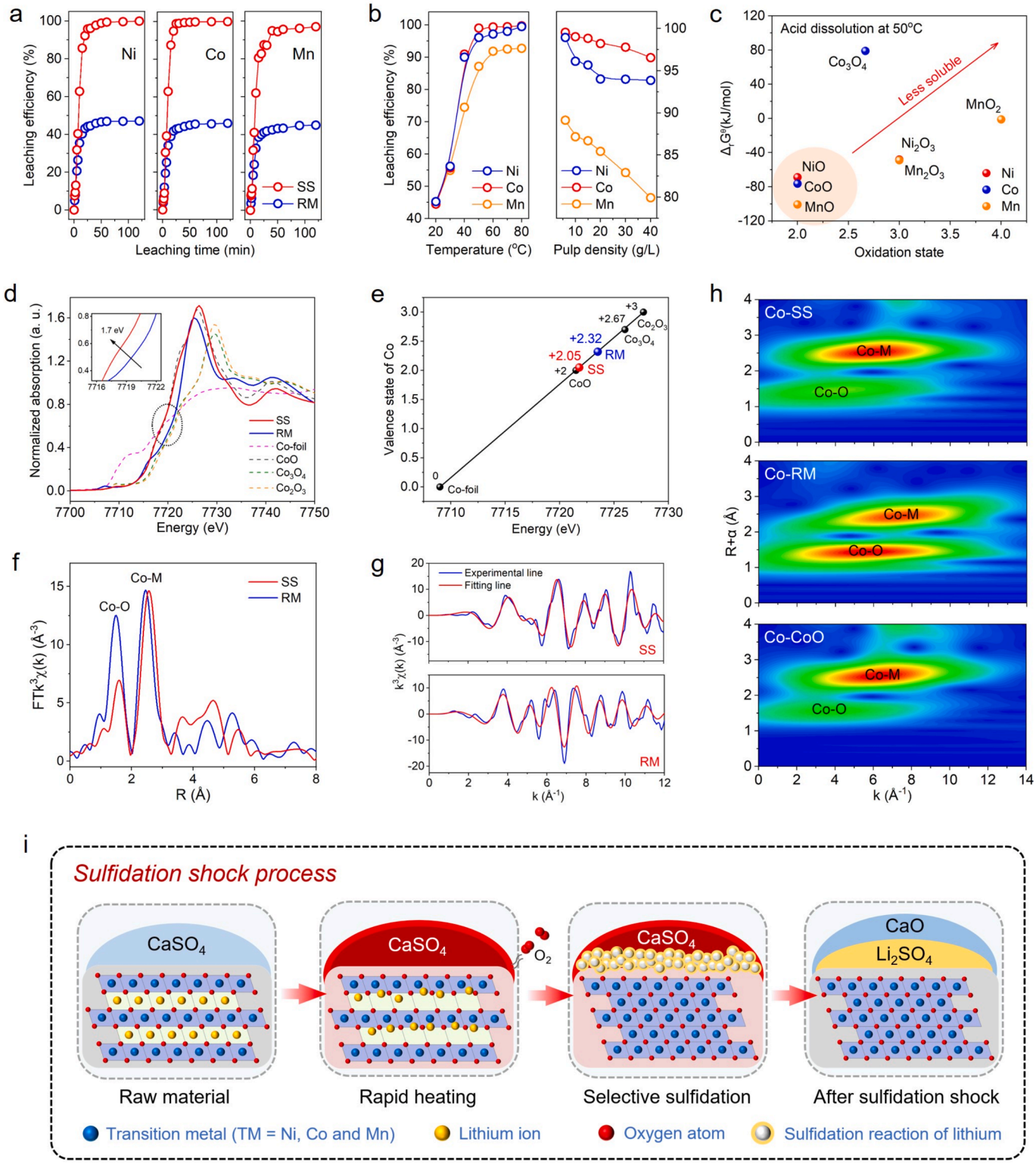

Fig. 4. Effect of (a) leaching time, (b) temperature, (c) pulp density on the acid leaching efficiency of TM metal (conditions: 50 °C, 0.5 M H_2SO_4, liquid–solid ratio of 20:1). (d) Gibbs free energy change of acid dissolution for TM metal compounds at 50 °C. (d) Co K-edge XANES of Co-SS, Co-RM and standard Co metal oxides. (e) Valence fitting analysis of Co atoms in Co-SS and Co-RM based on the maxima of the first derivative of XANES. (f) Fourier transform of EXAFS spectrum in R space and the best fitting result for Co-SS and Co-RM. (g) Fourier transform of EXAFS spectrum in K space and the best fitting result for Co-SS and Co-RM. (h) WT for the k^3-weighted EXAFS signals of Co-SS, Co-RM and Co_3O_4. (i) Schematic of the selective sulfidation of spent NCM.

In summary, the SS process can be described as follows (Fig. 4i): Li ions and lattice O in the layered octahedral unit quickly escape from the layered structure of cathode materials as the raw materials rapidly heat up while the Li^+ captures the escaping O_2 to form Li_2O. This process leads to the reduction of high-valence TMs to lower valence states due to the loss of lattice oxygen. Subsequently, Li_2O accumulating on the particle surface reacts with $CaSO_4$ through solid-phase interfacial contact to produce Li_2SO_4 according to Eq. (4).

$$Li_2O + CaSO_4 \rightarrow Li_2SO_4 + CaO \quad (4)$$

3.5. Environmental economic and scalability analysis

We designed three scenarios for recovering valuable metals from spent LIBs, as shown in Fig. 5a and S20-S22, including a pyrometallurgical process (Pyro), in which battery metals are transformed into alloys at approximately 1000 °C; a hydrometallurgical process (Hydro), which involves dissolving battery materials directly in acidic solvents; and the SS process, which converts battery materials into Li_2SO_4 and low-valence TM oxides. Assuming that a facility recycles 10,000 tons of spent NCM622 annually, we conducted a "cradle-to-gate" life cycle assessment for the three recovery scenarios using the EverBatt model. Since the SS process is based on Hydro, we referenced material consumption data for the SS process from the Hydro method outlined in the GREET 2020 inventory (Table S6). To account for the benefits of acid leaching for low-valence TMs in the SS products, we conservatively adjusted the H_2SO_4 consumption in the SS process to 80 % of that used in Hydro. In addition, the life cycle inventory of gypsum has been incorporated into the model [41], as detailed in Table S7.

Compared to Hydro, the SS process eliminated the use for hydrogen peroxide as a reductant, resulting in the upstream energy consumption for chemical production in the SS process was reduced by 33.2 % (Fig. 5c). Therefore, the total energy consumption of the SS process (14.77 MJ/kg cell) is lower than that of Hydro (22.12 MJ/kg cell). The lower consumption from the materials and energy inputs of the SS process results in greenhouse gas (GHG) emissions that are 57.3 % and 77.8 % of those from Pyro and Hydro processes, respectively (Fig. 5d and Table S8). In Pyro, Li reacts with flux materials (e.g., limestone and sand) to form a slag phase (xLi_2O-$yCaO$-zAl_2O_3-$nSiO_2$) with a complex composition and high melting/boiling points, making recovery of the dispersed Li extremely difficult [42,43]. Thus, Pyro generated the highest solid waste quantity among the three scenarios (Fig. 5b). The detailed environmental impact data are presented in Table S8. Moreover, the Li and TM leaching rates were approximately 6 % and 20 % higher in the SS process than in Hydro, respectively (data sourced from GREET 2020 and our experimental results), enhancing the value of metal products to give total revenues of 9.3 USD/kg cell for the SS process (Fig. 5e). Additionally, selective extraction during the SS process simplifies subsequent metal separation, leading to decreased overall energy and reagent consumption for recycling compared to the other

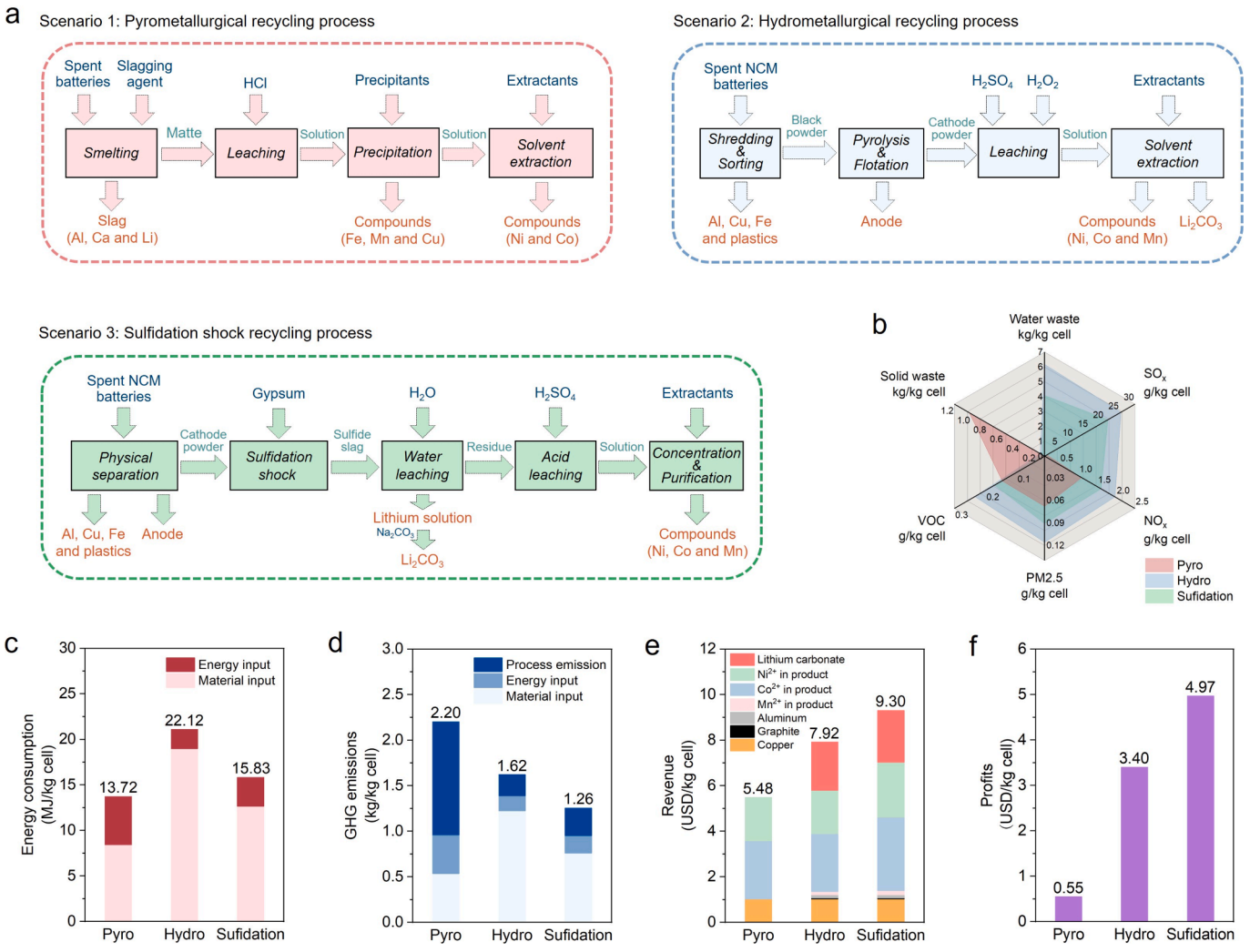

Fig. 5. (a) Materials flow analysis of the pyrometallurgy, hydrometallurgy and sulfidation shock recycling methods. Comparisons of (b) comprehensive pollutants, (c) total energy consumption, (d) greenhouse gas emission, (e) potential revenue and (f) prospective profits.

two scenarios. Finally, the projected profit for the SS process was 4.97 USD/kg cell due to the high metal recovery rates and low raw material costs, which was 9- and 1.5-fold greater than that of Pyro and Hydro, respectively (Fig. 5f and Tables S9-S10).

To demonstrate that the SS recycling process is scalable, we conducted scaled-up experiments of SS using a large-volume graphite boat, with a capable of 5 g of cathode powder (Fig. S23a-b). After thermal shocking treatment at a current intensity of 120 A and a duration of 30 s, the XRD pattern of SS products matched the result from the small-scale experiments (Fig. S23c). The SS products underwent a two-stage leaching process, which included water leaching followed by acid leaching, under the same leaching conditions used in the small-scale experiments. Fortunately, the leaching efficiencies for Li and TMs were maintained above 86 % and 93 %, respectively. The Li_2SO_4 in the water leachate was further prepared into Li_2CO_3 using the Na_2CO_3 precipitation method (Fig. S24). We also validated the universality of the SS method for battery metal extraction. The scaled-up experiments of SS were conducted on spent $LiCoO_2$ powder under optimum conditions. The XRD pattern indicate that $LiCoO_2$ was transformed into CoO and Li_2SiO_4 (Fig. S25). The leaching efficiencies of Li and Co were ~ 90 % and ~ 94 %, respectively. The SS recycling process has the potential to be integrated with a continuous feeding system, enabling continuous electrothermal sulfidation of cathode powder as shown in the conceptual design (Fig. S26). In addition, the graphene synthesis by the transient thermal process is increasingly being scaled up, and the productivity of tonnes per day has been achieved in 2024 [24]. This established scalability can be readily harnessed for high-throughput SS process.

4. Conclusion

In this work, we proposed a sulfidation shock method that employs Joule heat to selectively extract Li from battery metals while improving the leaching kinetics of TMs. The new method stimulated the ionic hopping of lattice Li in the cathode material and induced the migration of Li to the heat-stabilized sulfurizing agent on the cathode surface, which in turn constructed a sulfidation reaction interface without sulfur release. Meanwhile, the oxygen-loss reduction of TMs induced by transient high-temperature further promoted the leaching thermodynamics and avoids the use of reducing agents, such as hydrogen peroxide, in the acid leaching process. Unlike the energy-intensive conventional pyrometallurgical process, the rapid heating rate and short holding time of the sulfidation shock method resulted in only 0.23 % Li loss and a 42.7 % reduction in carbon emissions. Compared with the conventional hydrometallurgical technology, the new method increased Li and TMs recoveries by 6 % and 20 %, respectively, and increased economic benefits by 46.2 %. We believe that when further scaled up to kilogram or tonne scale, this method could allow the battery recycling industry to be built into a high-level demonstration of circular economy and cleaner production.

CRediT authorship contribution statement

Beikai Zhang: Writing – original draft, Data curation, Conceptualization. **Lanbin Wang:** Investigation, Formal analysis. **Duanmei Song:** Methodology. **Jing Wu:** Software. **Jiadong Yu:** Writing – review & editing, Funding acquisition. **Jinhui Li:** Writing – review & editing, Validation, Supervision, Funding acquisition.

Declaration of competing interest

The authors declare that they have no known competing financial interests or personal relationships that could have appeared to influence the work reported in this paper.

Acknowledgments

The authors are very grateful to Dr. Chongyao Li from Max Planck Institute for Polymer Research for her suggestions on the structure, logic, and drawing of this work. This research is supported by the National Natural Science Foundation of China (52300162 and 52270127).

Appendix A. Supplementary data

Supplementary data to this article can be found online at https://doi.org/10.1016/j.cej.2025.159206.

Data availability

No data was used for the research described in the article.

References

[1] Global EV Outlook 2024; IEA: Paris. https://www.iea.org/reports/global-ev-outlook-2024 (accessed 2024-04).
[2] F. Degen, M. Winter, D. Bendig, J. Tübke, Energy consumption of current and future production of lithium-ion and post lithium-ion battery cells, Nat. Energy 8 (2023) 1284–1295, https://doi.org/10.1038/s41560-023-01355-z.
[3] R. Shi, N. Zheng, H. Ji, M. Zhang, X. Xiao, J. Ma, W. Chen, J. Wang, H.M. Cheng, G. Zhou, Homogeneous Repair of Highly Degraded Ni-Rich Cathode Material with Spent Lithium Anode, Adv. Mater. 36 (2024), https://doi.org/10.1002/adma.202311553.
[4] Electric Vehicle Outlook 2024; BloombergNEF. https://about.bnef.com/electric-vehicle-outlook/ (accessed 2024-06).
[5] A. Ali, N. Bartie, J. Husmann, F. Cerdas, D. Schröder, C. Herrmann, Simulation-based life cycle assessment of secondary materials from recycling of lithium-ion batteries, Resour. Conserv. Recycl. 202 (2024) 107384, https://doi.org/10.1016/j.resconrec.2023.107384.
[6] X. Ma, M. Chen, Z. Zheng, D. Bullen, J. Wang, C. Harrison, E. Gratz, Y. Lin, Z. Yang, Y. Zhang, F. Wang, D. Robertson, S. Son, I. Bloom, J. Wen, M. Ge, X. Xiao, W. Lee, M. Tang, Q. Wang, J. Fu, Y. Zhang, B.C. Sousa, R. Arsenault, P. Karlson, N. Simon, Y. Wang, Recycled cathode materials enabled superior performance for lithium-ion batteries, Joule 5 (2021) 2955–2970, https://doi.org/10.1016/j.joule.2021.09.005.
[7] C. Stinn, A. Allanore, Selective sulfidation of metal compounds, Nature 602 (2022) 78–83, https://doi.org/10.1038/s41586-021-04321-5.
[8] J. Lin, C. Liu, H. Cao, R. Chen, Y. Yang, L. Li, Z. Sun, Environmentally benign process for selective recovery of valuable metals from spent lithium-ion batteries by using conventional sulfation roasting, Green Chem. 21 (2019) 594–5913, https://doi.org/10.1039/c9gc01350d.
[9] J. Lin, L. Li, E. Fan, C. Liu, X. Zhang, H. Cao, Z. Sun, R. Chen, Conversion Mechanisms of Selective Extraction of Lithium from Spent Lithium-Ion Batteries by Sulfation Roasting, ACS Appl. Mater. Interfaces 12 (2020) 18482–18489, https://doi.org/10.1021/acsami.0c00420.
[10] X. Zhang, L. Cai, E. Fan, J. Lin, F. Wu, R. Chen, L. Li, Recovery valuable metals from spent lithium-ion batteries via a low-temperature roasting approach: Thermodynamics and conversion mechanism, Journal of Hazardous Materials Advances 1 (2021) 100003, https://doi.org/10.1016/j.hazadv.2021.100003.
[11] Y. Tang, B. Zhang, H. Xie, X. Qu, P. Xing, H. Yin, Recovery and regeneration of lithium cobalt oxide from spent lithium-ion batteries through a low-temperature ammonium sulfate roasting approach, J. Power Sources 474 (2020) 228596, https://doi.org/10.1016/j.jpowsour.2020.228596.
[12] Y. Tang, X. Qu, B. Zhang, Y. Zhao, H. Xie, J. Zhao, Z. Ning, P. Xing, H. Yin, Recycling of spent lithium nickel cobalt manganese oxides via a low-temperature ammonium sulfation roasting approach, J. Clean. Prod. 279 (2021) 123633, https://doi.org/10.1016/j.jclepro.2020.123633.
[13] C. Yang, J. Zhang, Z. Cao, Q. Jing, Y. Chen, C. Wang, ꜱustainable and Facile Process for Lithium Recovery from Spent $LiNi_xCo_yMn_zO_2$ Cathode Materials via Selective Sulfation with Ammonium Sulfate, ACS Sustain. Chem. Eng. 8 (2020) 15732–15739, https://doi.org/10.1021/acssuschemeng.0c05676.
[14] D. Chang, S. Yang, P. Shi, Y. Jie, F. Hu, G. Fang, Y. Chen, Selective recovery of lithium and efficient leaching of transition metals from spent $LiNi_xCo_yMn_zO_2$ batteries based on a synergistic roasting process, Chem. Eng. J. 449 (2022) 137752, https://doi.org/10.1016/j.cej.2022.137752.
[15] F. Su, X. Zhou, X. Liu, Y. Ma, J. Tang, W. Yang, H. Wang, J. Yang, High-Efficiency Preferential Extraction of Lithium from Spent Lithium-Ion Battery Cathode Powder via Synergistic Treatment of Mechanochemical Activation and Oxidation Roasting, ACS Sustain. Chem. Eng. 11 (2023) 15685–15698, https://doi.org/10.1021/acssuschemeng.3c04752.
[16] W. Quan, K. Yan, Z. Zhang, H. Nie, R. Wang, Z. Xu, Novel targeted extraction of lithium: An environment-friendly controlled sulfidation roasting technology and mechanism for recovering spent lithium-ion batteries, Sep. Purif. Technol. 345 (2024) 127415, https://doi.org/10.1016/j.seppur.2024.127415.
[17] Y. Chen, P. Shi, D. Chang, Y. Jie, S. Yang, G. Wu, H. Chen, J. Zhu, F. Hu, B. P. Wilson, M. Lundstrom, Selective extraction of valuable metals from spent EV

power batteries using sulfation roasting and two stage leaching process, Sep. Purif. Technol. 258 (2021) 118078, https://doi.org/10.1016/j.seppur.2020.118078.
[18] Y. Zhong, Z. Li, J. Zou, T. Pan, P. Li, G. Yu, X. Wang, S. Wang, J. Zhang, A mild and efficient closed-loop recycling strategy for spent lithium-ion battery, J. Hazard. Mater. 474 (2024) 134794, https://doi.org/10.1016/j.jhazmat.2024.134794.
[19] A. Zhou, D. Zhang, Z. Liu, Z. Liu, Comprehensive recovery of valuable metals from spent $LiCoO_2$ cathode material by a method of NH_4HSO_4 roasting- $(NH_4)_2S$ leaching, Chem. Eng. J. 497 (2024) 154573, https://doi.org/10.1016/j.cej.2024.154573.
[20] C. Yang, Q. Wang, L. Xu, Y. Tian, Z. Zhao, Enhanced selective separation of valuable metals from spent lithium-ion batteries by aluminum synergistic sulfation roasting strategy, Sep. Purif. Technol. 345 (2024) 127279, https://doi.org/10.1016/j.seppur.2024.127279.
[21] K. Gu, X. Gao, Y. Chen, W. Qin, J. Han, Closed-loop recycling of spent lithium-ion batteries based on selective sulfidation: An unconventional approach, Waste Manage. 169 (2023) 32–42, https://doi.org/10.1016/j.wasman.2023.06.027.
[22] Q. Dong, T. Li, Y. Yao, X. Wang, S. He, J. Li, J. Luo, H. Zhang, Y. Pei, C. Zheng, M. Hong, H. Qiao, J. Gao, D. Wang, B. Yang, L. Hu, A General Method for Regenerating Catalytic Electrodes, Joule 4 (2020) 2374–2386, https://doi.org/10.1016/j.joule.2020.08.008.
[23] W. Chen, J. Chen, K.V. Bets, R.V. Salvatierra, K.M. Wyss, G. Gao, C.H. Choi, B. Deng, X. Wang, J.T. Li, C. Kittrell, N. La, L. Eddy, P. Scotland, Y. Cheng, S. Xu, B. Li, M.B. Tomson, Y. Han, B.I. Yakobson, J.M. Tour, Battery metal recycling by flash Joule heating, Sci. Adv. 9 (2023) eadh5131, https://doi.org/10.1126/sciadv.adh5131.
[24] Y. Cheng, J. Chen, B. Deng, W. Chen, K.J. Silva, L. Eddy, G. Wu, Y. Chen, B. Li, C. Kittrell, S. Xu, T. Si, A.A. Martí, B.I. Yakobson, Y. Zhao, J.M. Tour, Flash upcycling of waste glass fibre-reinforced plastics to silicon carbide, Nat. Sustain. 7 (2024) 452–462, https://doi.org/10.1038/s41893-024-01287-w.
[25] Y. Yao, Z. Huang, P. Xie, S.D. Lacey, R.J. Jacob, H. Xie, F. Chen, A. Nie, T. Pu, M. Rehwoldt, D. Yu, M.R. Zachariah, C. Wang, R. Shahbazian-Yassar, J. Li, L. Hu, Carbothermal shock synthesis of high-entropy-alloy nanoparticles, Science 359 (2018) 1489–1494, https://doi.org/10.1126/science.aan5412.
[26] B. Deng, D.X. Luong, Z. Wang, C. Kittrell, E.A. McHugh, J.M. Tour, Urban mining by flash Joule heating, Nat. Commun. 12 (2021) 5794, https://doi.org/10.1038/s41467-021-26038-9.
[27] X.H. Zhu, Y.J. Li, M.Q. Gong, R. Mo, S.Y. Luo, X. Yan, S. Yang, Recycling Valuable Metals from Spent Lithium-Ion Batteries Using Carbothermal Shock Method, Angew. Chem. Int. Ed. 62 (2023), https://doi.org/10.1002/anie.202300074.
[28] Q. Dai, J. Spangenberger, S. Ahmed, L. Gaines, J.C. Kelly, M. Wang, EverBatt: A Closed-loop Battery Recycling Cost and Environmental Impacts Model, United States (2019), https://doi.org/10.2172/1530874.
[29] Y. Ding, Y. Li, R. Xu, X. Han, K. Huang, X. Ke, B. Wang, M. Sui, P. Yan, Cross-scale deciphering thermal failure process of Ni-rich layered cathode, Nano Energy 126 (2024) 109685, https://doi.org/10.1016/j.nanoen.2024.109685.
[30] Y. Song, Y. Cui, B. Li, L. Geng, J. Yan, D. Zhu, P. Zhou, J. Zhou, Z. Yan, Q. Xue, Y. Tang, W. Xing, Revealing the origin of high-thermal-stability of single-crystal Ni-rich cathodes toward higher-safety batteries, Nano Energy 116 (2023) 108846, https://doi.org/10.1016/j.nanoen.2023.108846.
[31] C.W. Bale, E. Bélisle, P. Chartrand, S.A. Decterov, G. Eriksson, A.E. Gheribi, K. Hack, I.H. Jung, Y.B. Kang, J. Melançon, A.D. Pelton, S. Petersen, C. Robelin, J. Sangster, P. Spencer, M. Van Ende, FactSage thermochemical software and databases, 2010–2016, Calphad-Comput. Coupling Ph. Diagrams Thermochem. 54 (2016) 35–53, https://doi.org/10.1016/j.calphad.2016.05.002.
[32] J. Hu, J. Zhang, H. Li, Y. Chen, C. Wang, A promising approach for the recovery of high value-added metals from spent lithium-ion batteries, J. Power Sources 351 (2017) 192–199, https://doi.org/10.1016/j.jpowsour.2017.03.093.
[33] H. Huang, C. Liu, Z. Sun, In-situ pyrolysis based on alkaline medium removes fluorine-containing contaminants from spent lithium-ion batteries, J. Hazard. Mater. 457 (2023) 131782, https://doi.org/10.1016/j.jhazmat.2023.131782.
[34] K. Jia, J. Wang, Z. Zhuang, Z. Piao, M. Zhang, Z. Liang, G. Ji, J. Ma, H. Ji, W. Yao, G. Zhou, H. Cheng, Topotactic Transformation of Surface Structure Enabling Direct Regeneration of Spent Lithium-Ion Battery Cathodes, J. Am. Chem. Soc. 145 (2023) 7288–7300, https://doi.org/10.1021/jacs.2c13151.
[35] X. Liu, G. Xu, L. Yin, I. Hwang, Y. Li, L. Lu, W. Xu, X. Zhang, Y. Chen, Y. Ren, C. Sun, Z. Chen, M. Ouyang, K. Amine, Probing the Thermal-Driven Structural and Chemical Degradation of Ni-Rich Layered Cathodes by Co/Mn Exchange, J. Am. Chem. Soc. 142 (2020) 19745–19753, https://doi.org/10.1021/jacs.0c09961.
[36] K. Zhang, J. Qi, J. Song, Y. Zuo, Y. Yang, T. Yang, T. Chen, X. Liu, L. Chen, D. Xia, Sulfuration of Li-Rich Mn-Based Cathode Materials for Multianionic Redox and Stabilized Coordination Environment, Adv. Mater. 34 (2022), https://doi.org/10.1002/adma.202109564.
[37] L. Liang, M. Su, Z. Sun, L. Wang, L. Hou, H. Liu, Q. Zhang, C. Yuan, High-entropy doping promising ultrahigh-Ni Co-free single-crystalline cathode toward commercializable high-energy lithium-ion batteries, Sci. Adv. 10 (2024) eado4472, https://doi.org/10.1126/sciadv.ado4472.
[38] M. Zhang, L. Qiu, W. Hua, Y. Song, Y. Deng, Z. Wu, Y. Zhu, B. Zhong, S. Chou, S. Dou, Y. Xiao, X. Guo, Formulating Local Environment of Oxygen Mitigates Voltage Hysteresis in Li-Rich Materials, Adv. Mater. 36 (2024), https://doi.org/10.1002/adma.202311814.
[39] K.W. Nam, S.M. Bak, E. Hu, X. Yu, Y. Zhou, X. Wang, L. Wu, Y. Zhu, K.Y. Chung, X. Q. Yang, Combining In Situ Synchrotron X-Ray Diffraction and Absorption Techniques with Transmission Electron Microscopy to Study the Origin of Thermal Instability in Overcharged Cathode Materials for Lithium-Ion Batteries, Adv. Funct. Mater. 23 (2013) 1047–1063, https://doi.org/10.1002/adfm.201200693.
[40] S. Bak, K. Nam, W. Chang, X. Yu, E. Hu, S. Hwang, E.A. Stach, K. Kim, K.Y. Chung, X. Yang, Correlating Structural Changes and Gas Evolution during the Thermal Decomposition of Charged $Li_xNi_{0.8}Co_{0.15}Al_{0.05}O_2$ Cathode Materials, Chem. Mat. 25 (2013) 337–351, https://doi.org/10.1021/cm303096e.
[41] M.A. Pedreño-Rojas, J. Fořt, R. Černý, P. Rubio-de-Hita, Life cycle assessment of natural and recycled gypsum production in the Spanish context, J. Clean. Prod. 253 (2020) 120056, https://doi.org/10.1016/j.jclepro.2020.120056.
[42] H. Dang, B. Wang, Z. Chang, X. Wu, J. Feng, H. Zhou, W. Li, C. Sun, Recycled Lithium from Simulated Pyrometallurgical Slag by Chlorination Roasting, ACS Sustain. Chem. Eng. 6 (2018) 13160–13167, https://doi.org/10.1021/acssuschemeng.8b02713.
[43] J. Klimko, D. Oráč, A. Miškufová, C. Vonderstein, C. Dertmann, M. Sommerfeld, B. Friedrich, T. Havlík, A Combined Pyro- and Hydrometallurgical Approach to Recycle Pyrolyzed Lithium-Ion Battery Black Mass Part 2: Lithium Recovery from Li Enriched Slag—Thermodynamic Study, Kinetic Study, and Dry Digestion, Metals 10 (2020) 1558, https://doi.org/10.3390/met10111558.